Nanoscale

PAPER

View Article Online
View Journal | View Issue

Cite this: *Nanoscale*, 2023, **15**, 15656

Thermal self-reduction of metal hydroxide acrylate monolayer nanoparticles leads formation of nanoparticulate and porous structured alloys†

Naoki Tarutani, *[a,b] Yuka Hiragi,[a] Kengo Akashi,[a] Kiyofumi Katagiri [a] and Kei Inumaru [a]

Chemical and physical designs of alloy nanomaterials have attracted considerable attention for the development of highly functional materials. Although polyol processes using ionic precursors are widely used to synthesise alloy nanoparticles, the reduction potential of polyols limits their chemical composition, making it difficult to obtain 3d transition metals. In this study, we employed pre-synthesized metal hydroxide salt monolayer nanoparticles as precursors to obtain alloy nanoparticles. Simultaneous dehydroxylation of the hydroxide moiety and decomposition of the organic moiety allowed the formation of stable face-centred cubic metals passing through the metal carbide and metastable hexagonal close-packed metal phases. This self-reduction process enabled the formation of nanoparticulate bimetallic alloys and macroporous/mesoporous-structured bimetallic alloys by compositing hard/soft templates with pre-synthesized metal hydroxide salt nanoparticles. We believe that the strategy presented in this study can be used to design nanostructures and chemical compositions of multimetallic alloy nanoparticles as well as bimetallic systems.

Received 16th June 2023,
Accepted 14th September 2023

DOI: 10.1039/d3nr02876c

rsc.li/nanoscale

Introduction

Metal nanoparticles show improved and unique functions, such as depression of the melting point,[1,2] generation of a band gap,[3–5] surface plasmon resonance,[6–8] and crystal structure engineering,[9–11] compared to bulk materials. Alloying nanoparticles with two or more metal elements enables the fine tuning of their physical and chemical properties,[12,13] leading to unexpectedly high functionality in some cases.[14–16] Nanoparticles can be used as nano-building blocks (NBBs) to construct higher-order structures;[17,18] such as, assembled structures[19–21] and porous structures.[22]

The synthesis of metal nanoparticles through the chemical reduction of metal ion precursors is one of the most employed and successful techniques.[23] The chemical reduction of metal ions in a limited reaction space using reverse micelles has been used to prepare various metal nanoparticles, such as iron,[24] cobalt,[25] copper,[26] silver,[27,28] and bimetallic alloys.[29–31] However, there are limitations, such as poor crystallinity, low yield, and wide particle size distribution, to the reverse micelle approach.[32] Polyol process is another common approach to synthesize metal nanoparticles.[33] Polyols work as solvents and/or reducing agents. The injection of a metal salt solution into a pre-heated polyol medium results in the formation of metals. This process, called 'hot-injection', allow kinetic formation of metastable alloys composed of multielements.[15] The reduction potential of polyol is not enough to reduce 3d transition metals, such as cobalt and nickel; therefore, nanoparticles composed of such elements can be obtained by formation/decomposition of organometallic species in heated organic solvents.[34] In such cases, kinetical control to achieve alloy nanoparticle is difficult because the formation mechanism depends on the various parameters including counter anions and is complex even for pure metal nanoparticle formation.[35] Therefore, this study focused on a process that uses metal hydroxide salts as a precursor instead of ionic and organometallic species to synthesise alloy nanoparticles.

Metal hydroxide salts (MHS) are a family of layered double hydroxides. As shown in their general formula $M^{2+}(OH)_{2-x}(A^{m-})_{x/m}{\cdot}nH_2O$ (M = Mg^{2+}, Ca^{2+}, Co^{2+}, Ni^{2+}, Cu^{2+}, Zn^{2+}, *etc.*), MHS can incorporate various metal cation homogeneously in the atomic-scale.[36] Micrometre-sized MHS crystals form through typical inhomogeneous[37] and homogeneous[38] processes. In contrast, layered metal hydroxides are reported to obtain[39] through homogeneous basification by ring-

[a]*Applied Chemistry Program, Graduate School of Advanced Science and Engineering, Hiroshima University, 1-4-1 Kagamiyama, Higashi-Hiroshima, Hiroshima 739-8527, Japan. E-mail: n-tarutani@hiroshima-u.ac.jp*
[b]*Research Center for Micro-Nano Technology, Hosei University, 3-11-15 Midori-cho, Koganei, Tokyo 184-0003, Japan*

†Electronic supplementary information (ESI) available. See DOI: https://doi.org/10.1039/d3nr02876c

opening reaction of epoxides.[40] Further, we synthesised single-nanometre-sized crystalline MHS *via* epoxide-mediated basification.[41] Subsequently, we found that nanocrystalline nickel hydroxide malonates formed metallic nickel without generating any by-products after heat treatment in an inert atmosphere without an external supply of any reductive gas species. This result differs from those reported in other studies, wherein heat-treated MHS formed metal oxides[42–44] and metal/metal oxide composite.[45] In this study, we aimed to clarify the mechanism of metal-phase formation from MHS and applied the process to synthesize nanoparticulate and porous structured alloy materials.

Although metallic nickel was formed in our previous study, its size was greater than 100 nm.[41] Highly agglomerated condition of the precursor MHS nanoparticles is one of the reasons for coarse particle formation. In the following studies, well-dispersed MHS nanoparticles were obtained using monocarboxylates such as acetate instead of dicarboxylates such as malonate.[46–48] Acrylate was employed in this study to synthesise MHS monolayer nanoparticles composed of cobalt, nickel, and cobalt–nickel bimetals. *In situ* measurements using spectroscopic techniques revealed the successful formation of a solid-solution MHS. When a typical polyol reducing agent was used, alloy microparticles with an uncontrolled chemical composition were formed. In contrast, heat treatment of the MHS nanoparticles led to the formation of Co–Ni alloy nanoparticles with controlled chemical compositions. The formation mechanism of the metallic phase from MHS was investigated in detail, thereby enabling the synthesis of macroporous/mesoporous-structured alloys using the precursor MHS nanoparticles as NBBs.

Experimental

Chemicals

Cobalt chloride hexahydrate ($CoCl_2{\cdot}6H_2O$, 98.0%), nickel chloride hexahydrate ($NiCl_2{\cdot}6H_2O$, 98.0%), acrylic acid (99%), and propylene oxide (99.0%) were purchased from Sigma-Aldrich Co., LLC (St Louis, MO, USA). Ethanol (EtOH, 99.5%), ethylene glycol (EG, 99.5%), and tetrahydrofuran (THF, 98%) were purchased from Nacalai Tesque, Inc. (Kyoto, Japan). Polystyrene (PS) microparticle dispersion (PS-R-B1035, 5 wt% in H_2O, mean diameter of 508 nm, polydispersity index (PDI) of 0.02) was supplied by microParticles GmbH (Berlin-Adlershof, Germany). The block copolymer poly(styrene)-*b*-poly(ethylene oxide) (PS-*b*-PEO) (M_n = 18 000-*b*-7500, M_w/M_n = 1.05) was purchased from Polymer Source, Inc. (Dorval, Canada).

Synthesis of colloidal dispersions of cobalt, nickel, and cobalt–nickel hydroxide acrylate monolayer nanoparticles (Scheme S1a†)

$MCl_2{\cdot}6H_2O$ (M = Co or Ni) and acrylic acid were dissolved in EtOH (molar ratio of M : acrylic acid : EtOH = 1 : 2 : 34.25). Propylene oxide (15 molar equivalents against metal ions) was added to the solution and stirred for 30 s. Homogenous solutions were left in a water bath at a controlled temperature of 25 °C for 24 h. Colloidal dispersions were collected after rotary evaporation under 30 kPa at 30 °C for 5 min to remove the residual propylene oxide. The sample IDs are denoted as $Co_{1-x}Ni_xHA$, where x represents the nominal molar ratio of the cobalt and nickel salts dissolved in the starting solution.

Reduction of metal hydroxide acrylate nanoparticles through polyol process (Scheme S1b†)

The prepared colloidal dispersions were further rotary evaporated under 0.3 kPa 30 °C for 30 min after the addition of EG (EtOH : EG = 1 : 1 in volume) to replace the dispersion media from EtOH to EG. The 20 mL of colloidal dispersion in EG was added to the 150 mL of EG pre-heated at 190 °C with a dripping rate of ~2 mL min^{-1} (both solutions were bubbled with Ar for 15 min in advance). After stirring for 4 h, the precipitate was collected by centrifugation and washed with EtOH. The sample IDs are denoted as P-$Co_{1-x}Ni_xHA$.

Self-reduction of metal hydroxide acrylate monolayer nanoparticles (Scheme S1c†)

Powders were obtained after complete evaporation of $Co_{1-x}Ni_xHA$ dispersions by rotary evaporation under 0.3 kPa at 30 °C for 30 min. The powder (0.10 g) was placed in a quartz tube furnace in a quartz vessel. The furnace was vacuumed and refilled with Ar gas prior to heat treatment. Heat-treatment condition was 600 °C for 1 h with a ramp rate of 10 °C min^{-1} under Ar flow of 300 mL min^{-1}. The collected powders were denoted as SR-$Co_{1-x}Ni_xHA$.

Preparation of macroporous and mesoporous structured alloy materials

For macroporous structure formation, the as-received PS microparticle dispersion was diluted with EtOH (10 g L^{-1}) and allowed to dry in a glass Petri dish after ultrasonication. Formed polystyrene microparticle colloidal crystal was heated at 120 °C on the hot plate and 2 μL of as-synthesised $Co_{0.5}Ni_{0.5}HA$ dispersion was injected twice to form PS microparticles/$Co_{0.5}Ni_{0.5}HA$ composite. A block copolymer was used to form the mesoporous structures. PS-*b*-PEO (50 mg) was dissolved in 1.5 mL of THF at 40 °C, which allows formation of spherical micelle as reported previously.[49] $Co_{0.5}Ni_{0.5}HA$ dispersion of 2 mL was added to this solution. The obtained homogeneous dispersion was cast onto a Si substrate to form the PS-*b*-PEO micelles/$Co_{0.5}Ni_{0.5}HA$ composite. The obtained composites were heat-treated at 200 °C for 1 h in a pre-heated oven under air atmosphere and dipped in THF (40 °C) to remove PS microparticles or PS-*b*-PEO micelles. Further heat-treated at 600 °C for 1 h with a ramp rate of 10 °C min^{-1} under Ar flow of 300 mL min^{-1} for self-reduction.

Characterization

A field-emission scanning electron microscope (FE-SEM; S-4800, Hitachi High-Tech Corp., Tokyo, Japan) equipped with an energy-dispersive X-ray spectrometer (EDS) was used to observe the fine structures and investigate the elemental com-

position. A transmission electron microscope (TEM; JEM-2010, JEOL, Tokyo, Japan) equipped with an EDS was employed at an operating voltage of 200 kV to observe the nanoparticles. X-ray diffraction (XRD; D2 PHASER, Bruker AXS, Karlsruhe, Germany) using Cu Kα radiation was used to characterise the crystal phase of the powder samples. Fourier-transform infrared (FT-IR) spectroscopy (FT/IR-4100, JASCO, Tokyo, Japan) was used to characterise the chemical bonding states. Ultraviolet–visible (UV-Vis) spectroscopy (V-750; JASCO, Tokyo, Japan) was used to characterise the local structures of the solution samples. Small-angle X-ray scattering (SAXS) measurements were performed using a NANO-Viewer (Rigaku, Tokyo, Japan) equipped with a PILATUS 100k detector to evaluate the particle size in the dispersions. The fitting function of the SAXS pattern used to calculate the particle diameter is presented in the following section. *In situ* conductivity and pH data were collected every 5 s after the start of the reaction using a water quality meter (WQ-330J; Horiba, Japan). The relative amounts of ionic species were calculated using the following equation prepared from the calibration curve: $\sigma = 638 - c_{\mathrm{metal}}$, where σ and c_{metal} are the conductivity (10^{-3} S m^{-1}) of the solution and the concentration of metal ions (mol L^{-1}), respectively. Thermogravimetry-differential thermal analysis (TG-DTA; STA-449, Netzsch, Selb, Germany) combined with mass spectrometry (MS; JMS-Q1500GC, JEOL, Tokyo, Japan) was used to characterise the thermal behaviours of the samples and volatile products. The measurement conditions are as follows: temperature range of 40–700 °C, ramp rate of 10 °C min^{-1}, He gas flow of 50 mL min^{-1}, column temperature of 250 °C, and the m/z detecting range of 10–500. The chemical composition of formed alloy was determined using inductively coupled plasma optical emission spectroscopy (ICP-OES) (iCAP 6500, Thermo Fisher Scientific, Waltham, MA).

SAXS measurement

After removing the background scattering data for EtOH, the scattering 2D profiles were circularly averaged. To evaluate the particle size from the experimental SAXS patterns, we employed the unified equation proposed by Beaucage and Schaefer.[50,51] The unified equation for a monomodal structure is described as follows:

$$I(q) \approx G \exp\left(\frac{-q^2 {R_g}^2}{3}\right) + B\left\{\left[\mathrm{erf}\left(\frac{qR_g}{\sqrt{6}}\right)\right]\right\}^P,$$

where R_g is the gyration radius, P is the power-law exponent, G is the Guinier prefactor, and B is a prefactor specific to the type of power-law scattering. The particle diameter d_{SAXS} was calculated using the spherical particle model as follows:

$$R_g = \frac{d_{\mathrm{SAXS}}}{2}\sqrt{\frac{3}{5}}.$$

Results and discussion

Formation of solid solution nanoparticles of cobalt and nickel hydroxide acrylates

Epoxide is known to induce a pH increase in a solution of dissolved metal salts through an irreversible ring-opening reaction.[40] Fig. 1a shows the time-dependent potential change of the ethanolic reaction solution (the potential corresponds to pH in the case of an aqueous system). The potential, that is, proton activity, decreases with reaction time for all systems, indicating the basification of the solution. The relative amounts of metal ions decreased with reaction time (Fig. 1b). The timescale of the potential change and relative metal ion decrease were comparable in all the systems, which indicates that solids formed during basification of the solution. The relative ion amounts reached 0.033 (Co), 0.0023 (Ni), and 0.044 (Ni), indicating that the almost all the ions were consumed for all systems. Although Jobbágy *et al.* have reported formation of cobalt hydroxide and nickel hydroxide with a similar induction period in an aqueous solution using 3-hydroxypropylene oxide,[52] Ni system showed shorter induction period compared with Co system in this study. The difference might be derived from different structure of starting metal complexes. Water poor ethanolic condition with carboxylic acid leads formation of aqua-carboxylate complex.[46] Alkoxylation of nickel hydroxide have been reported under water poor synthetic condition

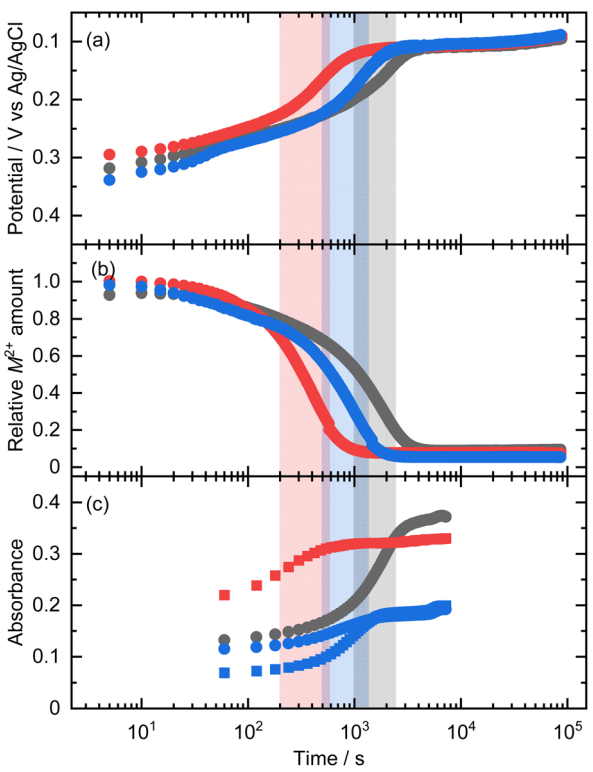

Fig. 1 Time-dependent change of (a) potential, (b) relative ion amounts, and (c) absorbance at 480 nm (circle, Co species) and 400 nm (square, Ni species) of reacting solutions of Co_1Ni_0HA (black), Co_0Ni_1HA (red), and $Co_{0.5}Ni_{0.5}HA$ (blue).

as well.[53] Considering these, starting metal complexes will have acrylate and/or ethoxy groups, which affects induction period of epoxide-mediated basification. The Co–Ni system exhibited an intermediate reaction rate and ion consumption rate between those of the Co and Ni systems. This implies the formation of a solid solution. The formation of solids (metal hydroxide salts) was evaluated by UV-vis spectroscopy. For both Co and Ni, the colour changed during the reaction due to changes in the coordinating ligands (Fig. S1†). The absorbance at a specific wavelength (480 nm for Co species and 400 nm for Ni species) was plotted against the reaction time to clarify the timescale of metal hydroxide salt formation (Fig. 1c). In the case of the Co and Ni systems, the absorbance changed around 1000–2500 s and 200–600 s, respectively, which is in good agreement with the timescale of potential change and ion consumption. On the other hand, the absorbances of both the Co and Ni species changed at comparable timescales of 500–1400 s after the start of the reaction in the case of Co–Ni system. This indicates that the Co and Ni species underwent co-hydrolysis and co-condensation to form a solid solution. This direct evidence of solid solution formation was achieved owing to low light scattering by nanoscale objects.

The diameters of the formed particles were estimated through SAXS and TEM. The SAXS pattern of $Co_{0.5}Ni_{0.5}HA$ was typical of monodispersed objects (Fig. 2a). The diameter of the dispersed object, d_{SAXS}, was calculated as 1.89 nm. Fig. 2a inset shows a TEM image of the formed particles. The mean diameters, d_{TEM}, was 1.74 (PDI of 0.14). The d_{SAXS} and d_{TEM} results are in good agreement. Although d_{SAXS} is slightly larger than d_{TEM}, this trend is due to the lower electron density of the acrylate moiety compared to that of the metal hydroxide moiety, as reported in our previous study.[47] The chemical composition of $Co_{0.5}Ni_{0.5}HA$ was estimated using TEM-EDS. The atomic ratio of Co : Ni was 0.47 : 0.53, which is comparable to the nominal molar ratio. The XRD patterns of the powdered samples are shown in Fig. 2b. The peak located at 2θ ~7.6° corresponds to the layered structures of metal hydroxide acrylates (lattice spacing of 1.17 nm (Co), 1.14 nm (Ni), and 1.15 nm (Co–Ni)) considering the reported studies.[46] The peaks derived from the lateral direction planes, such as 110, were not detected because of the small crystallite size and low crystallinity resulting from growth inhibition by the carboxylates.[41] A characteristic low-angle peak was not observed in the SAXS pattern, indicating that the synthesised $Co_{0.5}Ni_{0.5}HA$ was a monolayer nanoparticle dispersion, and a layered structural feature was observed owing to restacking during the drying of the dispersions. In conclusion, solid-solution Co–Ni hydroxide acrylates were obtained as monolayer nanoparticles through epoxide-mediated basification of solutions. Nanoparticle features provide direct evidence of solid-solution formation through *in situ* UV-vis analysis. The obtained Co–Ni hydroxide acrylates were used as precursors to synthesise the alloys.

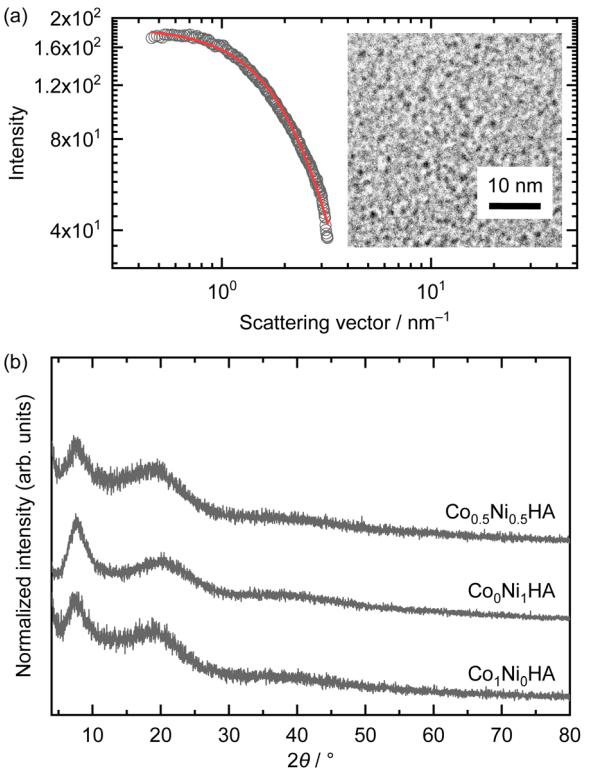

Fig. 2 (a) SAXS pattern of reacting solution of $Co_{0.5}Ni_{0.5x}HA$; raw data (black circle) and fitted data (red line). Inset is TEM image of dried $Co_{0.5}N_{0.5x}HA$. (b) XRD patterns of dried powders of Co_1Ni_0HA, Co_0Ni_1HA, and $Co_{0.5}Ni_{0.5}HA$.

Chemical reduction of metal hydroxide salts through polyol method towards alloy formation

Polyol process, which typically uses ethylene glycol as a reducing agent, is an efficient method for obtaining metal nanoparticles and microparticles.[33,54] Metal salts and hydroxides have been used as precursors to synthesise Co, Ni, Co–Ni alloys.[33,55–57] First, metal hydroxide salts are used as precursors for the polyol process. Fig. 3 shows SEM images of P-Co_1Ni_0HA, P-Co_0Ni_1HA, and P-$Co_{0.5}Ni_{0.5}HA$ obtained after reaction in ethylene glycol media at 190 °C for 4 h. Microparticles were formed in all systems. The XRD patterns reveal that the precipitates have face-cantered-cubic (fcc) crystal structures (Fig. S2a†). These results revealed that ethylene glycol successfully reduced the metal hydroxide salts to

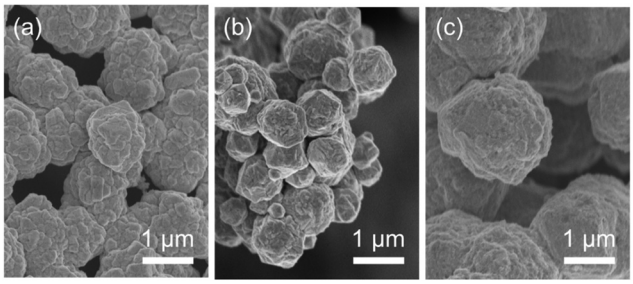

Fig. 3 SEM images of (a) P-Co_1Ni_0HA, (b) P-Co_0Ni_1HA, and (c) P-$Co_{0.5}Ni_{0.5}HA$.

metals. The calculated lattice constants of P-Co_1Ni_0HA, P-Co_0Ni_1HA, and P-$Co_{0.5}Ni_{0.5}$HA were 3.600(14) Å, 3.52357(15) Å, and 3.52206(68) Å, respectively (Fig. S2b†). The chemical composition of P-$Co_{0.5}Ni_{0.5}$HA was investigated using SEM-EDS, which revealed that the molar ratio of Co to Ni was 0.06 : 0.94. EDS mapping analysis revealed that both cobalt and nickel elements distributed homogeneously. The lattice constants of P-$Co_{1-x}Ni_x$HA well agree with Vegard's rule. These results indicate that formed P-$Co_{0.5}Ni_{0.5}$HA was Ni-rich Co–Ni alloy. The UV-vis spectrum of the supernatant showed that cobalt hydroxide salt species remained after the polyol process (Fig. S3†). Jeyadevan *et al.* suggested that the formation of metallic cobalt from cobalt hydroxide involves the replacement of hydroxyl ions with ethylene glycol monoanions to form intermediate metal alkoxides during the polyol process.[35] The reaction rate of metal alkoxide formation might differ between cobalt and nickel species, causing the formation of alloys with different chemical compositions compared with the precursor metal hydroxide acrylates.

Self-reduction of metal hydroxide salts through heat-treatment towards alloy formation

Self-reduction of metal hydroxide salts in an inert atmosphere was first reported by Gu *et al.* using nickel hydroxide cyanate.[45] They obtained a composite of metallic Ni and NiO. In contrast, we previously reported the formation of pure metallic Ni using nickel hydroxide malonate/succinate nanoparticles.[41,58] In this study, cobalt, nickel, and cobalt–nickel hydroxide acrylate nanoparticles were used for alloy formation. TG-MS was employed to investigate the thermal behaviour of Co_0Ni_1HA during heat treatment in an inert atmosphere (Fig. 4). The weight stared to decrease at ~100 °C owing to elimination of adsorbed water. The signal of m/z = 72 corresponding to acrylic acid was detected at 250–300 °C with slight weight loss, indicating the elimination of adsorbed acrylate species. Acrylate coordinated to nickel cation left even after heat-treatment at 300 °C confirmed by *ex situ* IR measurement (Fig. S4†). This indicates that the coordination to the metal hydroxide layer stabilises the organic moiety during heat treatment. Significant weight loss occurred at 300–400 °C. The detection of MS signals at m/z = 18 (H_2O), 28 (CO), and 44 (CO_2) indicates that the dehydration of the hydroxide moiety and decomposition of the acrylate moiety occurred in the same temperature range. Metallic Ni of fcc and hexagonal-close-packed (hcp) and Ni_3C formed at 400 °C. Although the metallic Ni hcp phase is known as the metastable phase, thermal decomposition of Ni_3C nanoparticles lead to the formation of an hcp phase.[59] According to the reported study,[60] the metallic Ni formed was considered as an interstitial-atom-free hcp phase. A small endothermic event at 450–490 °C and XRD patterns of sample heat-treated at 500 °C indicated decomposition of Ni_3C leaving fcc and hcp metallic Ni. After heat treatment at 600 °C for 1 h, the XRD pattern indicated the formation of a fcc Ni with trace hcp Ni. Decomposition of Ni_3C is known to leave amorphous or graphite-like carbon species.[61,62] Considering XRD pattern, amorphous carbon will form in this study. In summary, the heat treatment of nickel hydroxide acrylate triggers sequential and/or concerted dehydration of the hydroxide moiety and decomposition of the acrylate moiety to form Ni_3C, interstitial-atom-free hcp Ni, and fcc Ni subsequently. Thermal behaviours of Co_1Ni_0HA and $Co_{0.5}Ni_{0.5}$HA were investigated as well (Fig. S5†). Pure fcc Co phase was found to form at 600 °C through Co_2C and hcp Co intermediate phases. Although fcc metal phase formed at >400 °C in the case of $Co_{0.5}Ni_{0.5}$HA, intermediate crystalline carbide phase did not be detected. This implies that amorphous Co–Ni carbide formed.

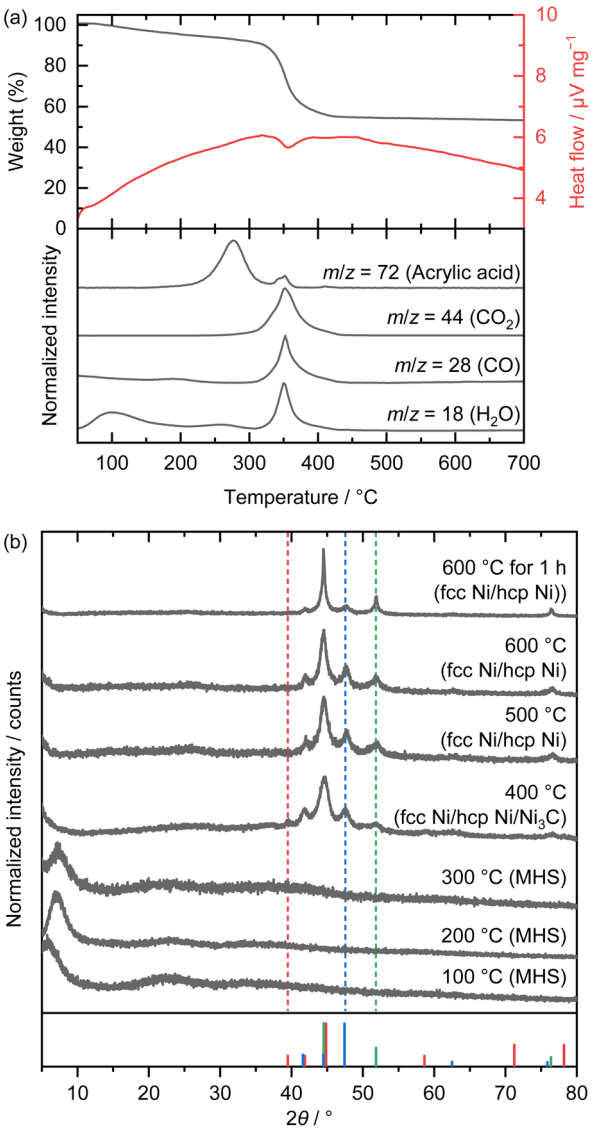

Fig. 4 (a) TG-DTA curves (upper panel) and MS spectra (lower panel) of Co_0Ni_1HA. (b) XRD patterns of Co_0Ni_1HA after heat-treatment at 100–600 °C without holding the temperature. The red, blue, and green bars in (b) are Ni_3C (JCPDS #06-0697), interstitial-atom-free hcp Ni[60] (analogous structure of hcp Co #89-7373), and fcc Ni (#04-0850).

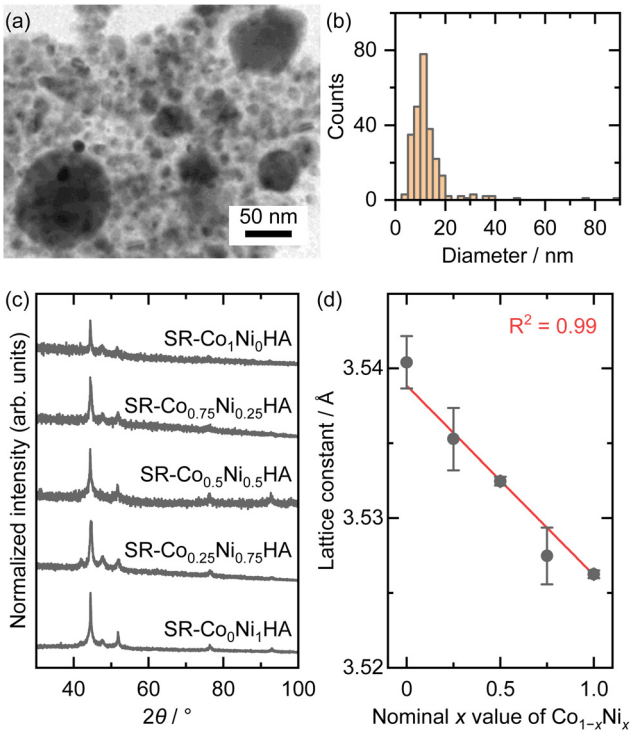

Fig. 5 (a) TEM images and (b) the corresponding particle diameter distribution of SR-$Co_{0.5}Ni_{0.5}$HA. (c) XRD patterns and (d) the corresponding lattice constants of SR-$Co_{1-x}Ni_x$HA (x = 0, 0.25, 0.5, 0.75, 1).

Considering the heat treatment conditions discussed above, $Co_{0.5}Ni_{0.5}$HA was heat-treated at 600 °C for 1 h in an inert atmosphere. Fig. 5a shows TEM images of SR-$Co_{0.5}Ni_{0.5}$HA. Nanoparticles with a size rage of 3.7–89 nm (average diameter of 12.8 nm) were observed. Electron diffraction pattern of nanoparticles was assigned as the fcc phase. The chemical composition of SR-$Co_{0.5}Ni_{0.5}$HA was determined as Co : Ni = 0.49 : 0.51 and 0.49 : 0.51 through macroscopic and microscopic analyses using SEM-EDS and TEM-EDS, respectively. ICP-OES technique was employed as well to determine chemical composition, which shows Co : Ni = 0.516 : 0.484. These values are comparable to that of the precursory $Co_{0.5}Ni_{0.5}$HA. SR-$Co_{1-x}Ni_x$HA (x = 0–1) was prepared under the same heat-treatment conditions. The XRD patterns indicate that the fcc-phase metals are the major components in all cases (Fig. 5c). The lattice constants of SR-Co_1Ni_0HA and SR-Co_0Ni_1HA are in good agreement with the reported values for the respective pure metals. SR-$Co_{1-x}Ni_x$HA (x = 0.25–0.75) showed a linear change in the lattice constant with the nominal chemical compositions (Fig. 5d), agreeing with Vegard's rule. Thus, the self-reduction reaction of metal hydroxide acrylates during heat treatment enables the formation of alloy nanoparticles without an external supply of reductive gas species. Here, a nanoparticle mixture of Co_1Ni_0HA and Co_0Ni_1HA was also heat-treated. Heat treated nanoparticle mixture showed comparable XRD pattern and corresponding lattice constant with SR-$Co_{0.5}Ni_{0.5}$HA (Fig. S6†). A solid-state reaction will be occurred during heat treatment as reported by Buonsanti *et al.*[63]

Nanoparticles with sizes on the single-nanometre scale have been reported to be used as nano-building blocks to construct not only macroporous structures but also mesoporous structures using hard- and soft-templates.[22,64,65] Although the robustness of the nanoparticle assembly is sometimes not sufficiently high to maintain porous structures, we have reported overcoming this issue by interconnecting nanoparticles through thermal polymerisation of the organic moiety of metal hydroxide acrylate.[66] For the macroporous structure, PS microparticles were used as hard templates (Fig. 6a). A colloidal crystal was obtained after evaporation-induced self-assembly of PS microparticles (Fig. S7†). Use of colloidal crystals as templates is known as one of the successful process toward inverse opal macroporous structure.[67] Nanoparticle dispersion of $Co_{0.5}Ni_{0.5}$HA were injected to the PS colloidal crystal and dried, which enabled to fill the interstitial spaces of PS microparticles. Formed PS/MHS nanoparticles composite was heat treated at 200 °C to induce thermal polymerization of acrylate moiety of MHS, which improves robustness of the MHS nanoparticles assembled skeleton. The removal of the PS microsphere template by dissolution in THF left well-oriented macropores with a diameter of ~400 nm is shown in Fig. 6b. Although the macropores shrank to ~200 nm in diameter owing to the volumetric loss during heat treatment at 600 °C for self-reduction, the porous structure was maintained (Fig. 6c). The PS-*b*-PEO micelles were used as soft templates for the formation of mesoporous structures (Fig. 6d). The dispersion, including $Co_{0.5}Ni_{0.5}$HA and PS-*b*-PEO, was cast onto the substrate, allowing co-assembly through an evaporation-induced self-assembly process. Obtained micelles/MHS nanoparticles composite was heat treated at 200 °C to improve robustness of the MHS nanoparticle assembled skeleton. A mesoporous structure with a pore diameter of ~30 nm was obtained after removing the PS-*b*-PEO template by dissolution in THF (Fig. 6d). The mesopore size was comparable to a reported value,[49] indicating that spherical micelles of PS-*b*-PEO were successfully formed during the evaporation process. The mesoporous structure was maintained even after self-reduction although nanoscale cracks were formed (Fig. 6e). The mesopore size was comparable before and after self-reduction, despite the volumetric loss. This is due to unidirectional contraction, which is known to occur in the case of mesoporous films immobilised on the substrate.[68] Different to alloy nanoparticles prepared without any templates (Fig. 5a), large nanoparticles with a size greater than 50 nm did not form in both porous structured cases. Spatial disconnections by the introduced pores may limit the diffusion of atoms and inhibit particle growth. The strategy shown here using inorganic–organic hybrid metal hydroxide salt nanoparticles as precursors for the synthesis of alloys is successful not only in designing the chemical composition of the synthesised alloy nanoparticles but also for structural control at the macro/meso-scales.

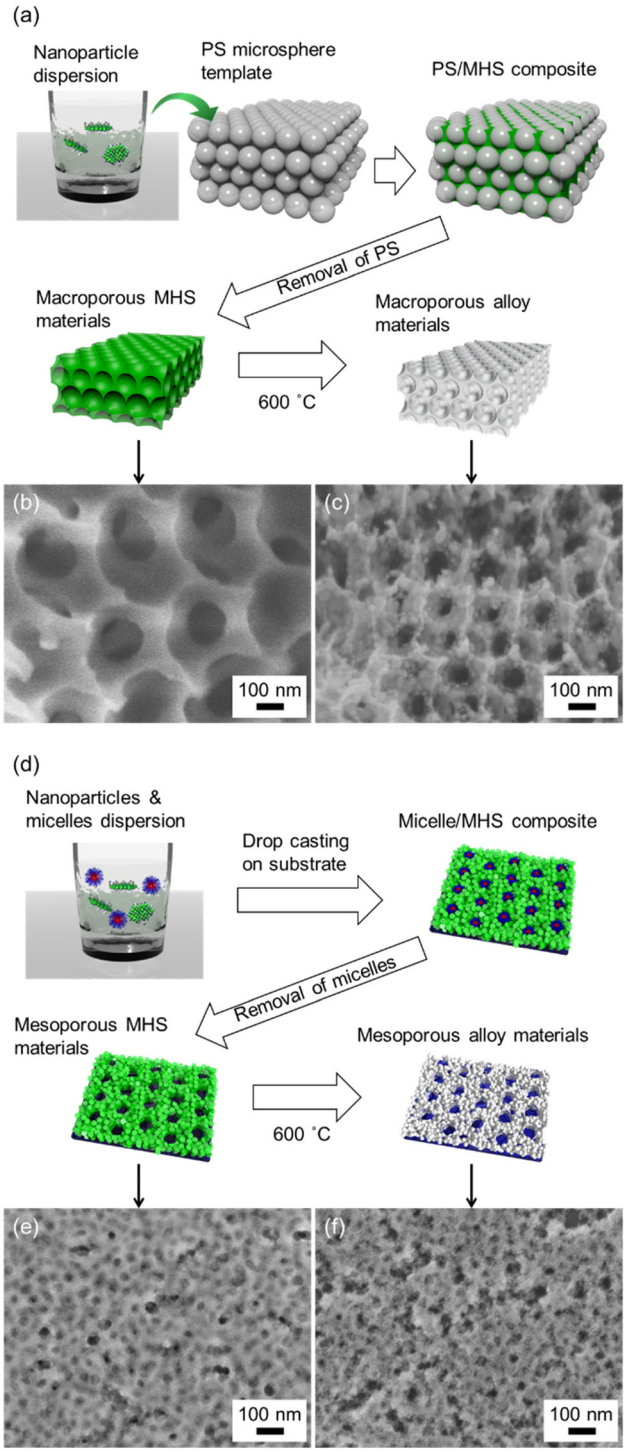

Fig. 6 Schematic illustration of (a) macroporous and (d) mesoporous alloy materials. SEM images of (b) and (c) macroporous and (e) and (f) mesoporous structures composed of (b) and (e) Co–Ni MHS and (c) and (f) Co–Ni alloy, respectively.

Conclusions

This study demonstrated a novel strategy to synthesise alloy materials with controlled shapes, such as, nanoparticles, mesoporous structures, and macroporous structures, using metal hydroxide acrylate nanoparticles. The formation of a solid solution of metal hydroxide acrylates was demonstrated using an *in situ* spectroscopic technique because of the low light-scattering property of the nano-object. Alloy microparticles of Co–Ni with an uncontrolled chemical composition were prepared using the traditional polyol method. In contrast, Co–Ni alloy nanoparticles with a well-controlled chemical composition were formed by the heat treatment of metal hydroxide acrylate monolayer nanoparticles. *In situ* and *ex situ* measurements revealed that metallic Co, Ni, and Co–Ni alloy was formed *via* the self-reduction of metal hydroxide acrylates, including the formation and decomposition of the metal carbides. Owing to the small size of the precursory metal hydroxide acrylate nanoparticles, composites with hard and soft templates were successfully prepared. Well-defined macroporous/mesoporous structures were formed after the removal of the templates and self-reduction reaction. The approach shown here is expected to be employed to synthesise bimetallic alloys as well as complex alloys.

Conflicts of interest

There are no conflicts to declare.

Acknowledgements

This work was partially supported by JSPS KAKENHI grant numbers JP18H01709, JP20H02439, JP20K15368, JP21H00149, JP22K14753, JP22H05143, and JP23H00236, JST FOREST program grant number JPMJFR221W, and the JST Core-to-Core program. We also thank MEXT Leading Initiative for Excellent Young Researchers, MEXT Strategic Professional Development Program for Young Researchers (HIRAKU-Global), Iketani Science and Technology Foundation (0331128-A), Takahashi Industrial and Economic Research Foundation (11-003-402), The Mazda Foundation, and the Cooperative Research Program of Institute for Catalysis, Hokkaido University, the facilities of the Institute of Materials and Systems for Sustainability, Nagoya University.

References

1 P. Buffat and J. P. Borel, *Phys. Rev. A*, 1976, **13**, 2287–2298.
2 A. van Teijlingen, S. A. Davis and S. R. Hall, *Nanoscale Adv.*, 2020, **2**, 2347–2351.
3 S. B. DiCenzo, S. D. Berry and E. H. Hartford, *Phys. Rev. B: Condens. Matter Mater. Phys.*, 1988, **38**, 8465–8468.
4 T. Stoll, E. Sgro, J. W. Jarrett, J. Rehault, A. Oriana, L. Sala, F. Branchi, G. Cerullo and K. L. Knappenberger Jr., *J. Am. Chem. Soc.*, 2016, **138**, 1788–1791.
5 B. L. Han, Z. Liu, L. Feng, Z. Wang, R. K. Gupta, C. M. Aikens, C. H. Tung and D. Sun, *J. Am. Chem. Soc.*, 2020, **142**, 5834–5841.

6 T. Klar, M. Perner, S. Grosse, G. von Plessen, W. Spirkl and J. Feldmann, *Phys. Rev. Lett.*, 1998, **80**, 4249–4252.
7 H. Yu, Y. Peng, Y. Yang and Z.-Y. Li, *npj Comput. Mater.*, 2019, **5**, 45.
8 S. Li, P. Miao, Y. Zhang, J. Wu, B. Zhang, Y. Du, X. Han, J. Sun and P. Xu, *Adv. Mater.*, 2021, **33**, e2000086.
9 Y. Chen, Z. Lai, X. Zhang, Z. Fan, Q. He, C. Tan and H. Zhang, *Nat. Rev. Chem.*, 2020, **4**, 243–256.
10 K. Matsumoto, R. Sato, Y. Tatetsu, R. Takahata, S. Yamazoe, M. Yamauchi, Y. Inagaki, Y. Horibe, M. Kudo, T. Toriyama, M. Auchi, M. Haruta, H. Kurata and T. Teranishi, *Nat. Commun.*, 2022, **13**, 1047.
11 K. Matsumoto, R. Sato and T. Teranishi, *Trends Chem.*, 2023, **5**, 201–213.
12 P.-C. Chen, X. Liu, J. L. Hedrick, Z. Xie, S. Wang, Q.-Y. Lin, M. C. Hersam, V. P. Dravid and C. A. Mirkin, *Science*, 2016, **352**, 1565–1569.
13 L. Huang, M. Liu, H. Lin, Y. Xu, J. Wu, V. P. Dravid, C. Wolverton and C. A. Mirkin, *Science*, 2019, **365**, 1159–1163.
14 Y. Yao, Z. Huang, P. Xie, S. D. Lacey, R. J. Jacob, H. Xie, F. Chen, A. Nie, T. Pu, M. Rehwoldt, D. Yu, M. R. Zachariah, C. Wang, R. Shahbazian-Yassar, J. Li and L. Hu, *Science*, 2018, **359**, 1489–1494.
15 D. Wu, K. Kusada, T. Yamamoto, T. Toriyama, S. Matsumura, S. Kawaguchi, Y. Kubota and H. Kitagawa, *J. Am. Chem. Soc.*, 2020, **142**, 13833–13838.
16 D. Wu, K. Kusada, Y. Nanba, M. Koyama, T. Yamamoto, T. Toriyama, S. Matsumura, O. Seo, I. Gueye, J. Kim, L. S. Rosantha Kumara, O. Sakata, S. Kawaguchi, Y. Kubota and H. Kitagawa, *J. Am. Chem. Soc.*, 2022, **144**, 3365–3369.
17 M. Niederberger, *Adv. Funct. Mater.*, 2017, **27**, 1–18.
18 Z. Xue, C. Yan and T. Wang, *Adv. Funct. Mater.*, 2019, **29**, 1–33.
19 S. Rao, K. J. Si, L. W. Yap, Y. Xiang and W. Cheng, *ACS Nano*, 2015, **9**, 11218–11224.
20 K. Deng, Z. Luo, L. Tan and Z. Quan, *Chem. Soc. Rev.*, 2020, **49**, 6002–6038.
21 M. Grzelczak, L. M. Liz-Marzan and R. Klajn, *Chem. Soc. Rev.*, 2019, **48**, 1342–1361.
22 S. C. Warren, L. C. Messina, L. S. Slaughter, M. Kamperman, Q. Zhou, S. M. Gruner, F. J. DiSalvo and U. Wiesner, *Science*, 2008, **320**, 1748–1752.
23 J. Park, J. Joo, G. K. Soon, Y. Jang and T. Hyeon, *Angew. Chem., Int. Ed.*, 2007, **46**, 4630–4660.
24 A. A. Revina, O. V. Suvorova, Y. S. Pavlov and D. L. Tytik, *Prot. Met. Phys. Chem. Surf.*, 2019, **55**, 888–894.
25 C. Petit, A. Taleb and M.-P. Pileni, *Adv. Mater.*, 1998, **10**, 259–261.
26 M. P. Pileni, B. W. Ninham, T. Gulik-Krzywicki, J. Tanori, I. Lisiecki and A. Filankembo, *Adv. Mater.*, 1999, **11**, 1358–1362.
27 M. Maillard, S. Giorgio and M. P. Pileni, *Adv. Mater.*, 2002, **14**, 1084–1084.
28 P. S. Popovetskiy and D. I. Beketova, *Colloids Surf., A*, 2019, **568**, 51–58.
29 C. Tojo, D. Buceta and M. A. Lopez-Quintela, *J. Colloid Interface Sci.*, 2018, **510**, 152–161.
30 M. O. Sergeev, A. A. Revina, O. A. Boeva, K. N. Zhavoronkova and V. I. Zolotarevskii, *Prot. Met. Phys. Chem. Surf.*, 2020, **56**, 63–74.
31 M. O. Sergeev, A. A. Revina and O. V. Suvorova, *Prot. Met. Phys. Chem. Surf.*, 2021, **57**, 516–524.
32 D. Ingert and M. P. Pileni, *Adv. Funct. Mater.*, 2001, **11**, 136–139.
33 F. Fievet, J. Lagier, B. Blin, B. Beaudoin and M. Figlarz, *Solid State Ionics*, 1989, **32–33**, 198–205.
34 K. Taniguchi, K. Shinoda, J. L. Cuya Huaman, S. Yokoyama, M. Uchikoshi, T. Matsumoto, K. Suzuki, H. Miyamura and B. Jeyadevan, *SN Appl. Sci.*, 2019, **1**, 124–124.
35 T. Matsumoto, K. Takahashi, K. Kitagishi, K. Shinoda, J. L. Cuya Huaman, J.-Y. Piquemal and B. Jeyadevan, *New J. Chem.*, 2015, **39**, 5008–5018.
36 G. G. C. Arizaga, K. G. Satyanarayana and F. Wypych, *Solid State Ionics*, 2007, **178**, 1143–1162.
37 R. Marangoni, G. A. Bubniak, M. P. Cantão, M. Abbate, W. H. Schreiner and F. Wypych, *J. Colloid Interface Sci.*, 2001, **240**, 245–251.
38 L. Poul, N. Jouini and F. Fievet, *Chem. Mater.*, 2000, **12**, 3123–3132.
39 V. Oestreicher and M. Jobbagy, *Langmuir*, 2013, **29**, 12104–12109.
40 A. E. Gash, T. M. Tillotson, J. H. Satcher, J. F. Poco, L. W. Hrubesh and R. L. Simpson, *Chem. Mater.*, 2001, **13**, 999–1007.
41 N. Tarutani, Y. Tokudome, M. Jobbágy, F. A. Viva, G. J. A. A. Soler-Illia and M. Takahashi, *Chem. Mater.*, 2016, **28**, 5606–5610.
42 P. Bénard, J. P. Auffrédic and D. Louër, *Thermochim. Acta*, 1994, **232**, 65–76.
43 N. Guillou, M. Louër and D. Louër, *J. Solid State Chem.*, 1994, **109**, 307–314.
44 L. Markov, K. Petrov and V. Petkov, *Thermochim. Acta*, 1986, **106**, 283–292.
45 X. Ge, C. D. Gu, X. L. Wang and J. P. Tu, *Chem. Commun.*, 2015, **51**, 1004–1007.
46 N. Tarutani, Y. Tokudome, M. Jobbagy, G. J. A. A. Soler-Ilia, Q. Y. Tang, M. Muller and M. Takahashi, *Chem. Mater.*, 2019, **31**, 322–330.
47 N. Tarutani, S. Kimura, T. Sakata, K. Suzuki, K. Katagiri and K. Inumaru, *ACS Mater. Lett.*, 2022, **4**, 1430–1435.
48 N. Tarutani, Y. Tokudome, M. Jobbágy, G. J. A. A. Soler-Illia and M. Takahashi, *J. Mater. Chem. A*, 2019, **7**, 25290–25296.
49 X. Jiang, N. Suzuki, B. P. Bastakoti, W. J. Chen, Y. T. Huang and Y. Yamauchi, *Eur. J. Inorg. Chem.*, 2013, **2013**, 3286–3291.
50 G. Beaucage and D. W. Schaefer, *J. Non. Cryst. Solids*, 1994, **172–174**, 797–805.
51 G. Beaucage, *J. Appl. Crystallogr.*, 1995, **28**, 717–728.
52 V. Oestreicher, I. Fábregas and M. Jobbágy, *J. Phys. Chem. C*, 2014, **118**, 30274–30281.

53 K. Muramatsu, Y. Kuroda, H. Wada, A. Shimojima and K. Kuroda, *Inorg. Chem.*, 2021, **60**, 7094–7100.
54 F. Fiévet, S. Ammar-Merah, R. Brayner, F. Chau, M. Giraud, F. Mammeri, J. Peron, J. Y. Piquemal, L. Sicard and G. Viau, *Chem. Soc. Rev.*, 2018, **47**, 5187–5233.
55 F. Fievet, J. P. Lagier and M. Figlarz, *MRS Bull.*, 1989, **14**, 29–34.
56 P. Saravanan, T. A. Jose, P. J. Thomas and G. U. Kulkarni, *Bull. Mater. Sci.*, 2001, **24**, 515–521.
57 S. Panday, B. S. S. Daniel and P. Jeevanandam, *J. Magn. Magn. Mater.*, 2011, **323**, 2271–2280.
58 N. Tarutani, K. Akashi, K. Katagiri and K. Inumaru, *Inorg. Chem.*, 2023, **62**, 13977–13984.
59 Z. L. Schaefer, K. M. Weeber, R. Misra, P. Schiffer and R. E. Schaak, *Chem. Mater.*, 2011, **23**, 2475–2480.
60 R.-T. Chiang, R.-K. Chiang and F.-S. Shieu, *RSC Adv.*, 2014, **4**, 19488–19488.
61 Y. Leng, L. Xie, F. Liao, J. Zheng and X. Li, *Thermochim. Acta*, 2008, **473**, 14–18.
62 Z. L. Schaefer, M. L. Gross, M. A. Hickner and R. E. Schaak, *Angew. Chem., Int. Ed.*, 2010, **49**, 7045–7048.
63 C. Gadiyar, A. Loiudice, F. D'Ambra, E. Oveisi, D. Stoian, P. Iyengar, L. Castilla-Amorós, V. Mantella and R. Buonsanti, *J. Am. Chem. Soc.*, 2020, **142**, 15931–15940.
64 M. S. Wong, E. S. Jeng and J. Y. Ying, *Nano Lett.*, 2001, **1**, 637–642.
65 J. Wang, Q. Li, W. Knoll and U. Jonas, *J. Am. Chem. Soc.*, 2006, **128**, 15606–15607.
66 N. Tarutani, R. Sato, W. Yamazaki, K. Katagiri, K. Inumaru and T. Ishigaki, *Nanoscale*, 2021, **13**, 11446–11454.
67 A. Stein, F. Li and N. R. Denny, *Chem. Mater.*, 2007, **20**, 649–666.
68 D. Grosso, G. J. A. A. De Soler-Illia, F. Babonneau, C. Sanchez, P. A. Albouy, A. Brunet-Bruneau and A. R. Balkenende, *Adv. Mater.*, 2001, **13**, 1085–1090.